Stabilization of Unsteady Nonlinear Waves by Phase-Space Manipulation

Alexis Gomel,[1,2] Amin Chabchoub,[3,4,5] Maura Brunetti,[1,2] Stefano Trillo,[6]
Jérôme Kasparian,[1,2,*] and Andrea Armaroli[1,2,†]

[1]GAP, Université de Genève, Chemin de Pinchat 22, 1227 Carouge, Switzerland
[2]Institute for Environmental Sciences, Université de Genève, Boulevard Carl-Vogt 66, 1205 Genève, Switzerland
[3]Hakubi Center for Advanced Research, Kyoto University, Yoshida-Honmachi, Kyoto 606-8501, Japan
[4]Disaster Prevention Research Institute, Kyoto University, Uji, Kyoto 611-0011, Japan
[5]Centre for Wind, Waves and Water, School of Civil Engineering, The University of Sydney, Sydney, NSW 2006, Australia
[6]Department of Engineering, University of Ferrara, via Saragat 1, 44122 Ferrara, Italy

(Received 9 September 2020; revised 23 February 2021; accepted 1 April 2021; published 27 April 2021)

We introduce a dynamic stabilization scheme universally applicable to unidirectional nonlinear coherent waves. By abruptly changing the waveguiding properties, the breathing of wave packets subject to modulation instability can be stabilized as a result of the abrupt expansion a homoclinic orbit and its fall into an elliptic fixed point (center). We apply this concept to the nonlinear Schrödinger equation framework and show that an Akhmediev breather envelope, which is at the core of Fermi-Pasta-Ulam-Tsingou recurrence and extreme wave events, can be *frozen* into a steady periodic (dnoidal) wave by a suitable variation of a single external physical parameter. We experimentally demonstrate this general approach in the particular case of surface gravity water waves propagating in a wave flume with an abrupt bathymetry change. Our results highlight the influence of topography and waveguide properties on the lifetime of nonlinear waves and confirm the possibility to control them.

DOI: 10.1103/PhysRevLett.126.174501

The parametric stabilization of unstable dynamics is a fascinating and long-standing problem, the paradigmatic example being the Kapitza pendulum [1], i.e., the dynamic stabilization of a pendulum around its inverted position by fast oscillating its pivot.

Dynamic stabilization is still effective for nonlinear and dispersive waves which are intrinsically infinite dimensional, unlike nonlinear control theory and feedback schemes. Applications range from dispersion management in fiber laser and communications [2] to control of nonlinear waves in many-body quantum physics [3], diffractive optics [4], matter waves [5], or water waves [6]. However, dynamic stabilization requires a spatially *extended* periodicity, and alternative stabilization and control schemes of nonlinear waves are needed [7].

Here, we introduce theoretically and validate experimentally such a nonlinear wave stabilization based on abruptly changing the propagation conditions, expanding a phase-space trajectory homoclinic to a saddle point [8,9]. Generically, this trajectory contains a family of closed orbits, converging to a single point known as center. The phase-space manipulation stabilizes the system evolution around the center, suddenly *freezing* the growth stage of a breather wave envelope at its peak height.

Unlike Kapitza or feedback schemes, such an expansion is induced by a controlled, local and abrupt variation of a single parameter affecting both the nonlinearity and the dispersion of the wave system. As an example, we apply this concept to unidirectional water surface gravity waves subject to the ubiquitous phenomenon of modulational instability (MI) of Stokes waves or Benjamin-Feir instability [10–13]. The evolution of such unstable waves can be described by the universal nonlinear Schrödinger equation (NLSE) [14]. MI entails the exponential growth of a slow modulation on top of a carrier wave of uniform amplitude possibly yielding to the formation of extreme waves. Remarkably, the continuation of MI in the fully nonlinear (strongly depleted) stage as modeled by Akhmediev breathers (ABs) is equivalent to a homoclinic pendulumlike phase-space structure [15–19], where the background behaves as a saddle point, while two centers are represented by two out of phase stationary periodic wave envelopes, the dnoidal solutions of the NLSE [20,21]. The unstable AB orbit describes the amplification of sidebands up to a peak and the asymptotic return to the background [22]. Since it separates two qualitatively different types of periodic evolutions undergoing Fermi-Pasta-Ulam-Tsingou (FPUT) recurrences, the AB is a separatrix in the wave system phase space [19,23,24].

We demonstrate the possibility to stabilize such an unstable homoclinic orbit by matching it to one of the steady dnoidal solutions. The matching is strictly forbidden by the Hamiltonian structure of the NLSE for unperturbed MI evolutions. Instead, we parametrically perturb the system by abruptly (i.e., faster than the MI characteristic distance) increasing the water depth and, thus, changing the dispersion and nonlinearity experienced by the envelope.

This causes a strong dilation of the AB orbit at its apex and, ideally, the fall of the trajectory over the center (dnoidal envelope). This blocks the FPUT recurrence and *freezes* the breather at its peak.

The proposed *separatrix dilation* is somehow opposite to the common phenomena of wave shoaling responsible for the increase of wave amplitude, typical for the depth decrease in coastal areas [25–28]. On the other hand, an increase of water depth in the direction of wave propagation can still occur in the ocean, mostly in surf zones like sandbars and coral reefs. The present mechanism can also occur where the NLSE provides a leading-order description of nonlinear MI, such as Bose-Einstein condensation [29] and optics, where quasi-stabilization has been interpreted in terms of solitons [30]. Indeed, this approach can be extended to other models with a homoclinic structure [31], and even to settings such as parametric resonance described by strongly nonintegrable models [32].

A NLSE-like equation was derived for the one-dimensional and unidirectional evolution of the envelope of surface water waves on an uneven bottom of depth h at frequency $\omega = \sqrt{gk\sigma}$, with $\sigma \equiv \tanh\kappa$ and $\kappa \equiv kh$, k being the local wave number, which varies with h, while ω is fixed [26]. The slope of the depth step in the propagation direction x should be sufficiently small to prevent wave reflections due to wave number mismatches: $h'(x) = \mathcal{O}(\varepsilon^2)$, with $\varepsilon \equiv ka$ the wave steepness, a being the carrier wave amplitude. Applying the method of multiple scales up to $\mathcal{O}(\varepsilon^3)$ to the inviscid irrotational water wave problem yields the evolution equation [26,33],

$$i\frac{\partial V}{\partial \xi} + \beta\frac{\partial^2 V}{\partial \tau^2} - \tilde{\gamma}|V|^2 V = 0, \tag{1}$$

where $V(\xi,\tau)$ is the shoaling-corrected envelope of the free-surface elevation [34,35], $\xi \equiv \varepsilon^2 x$, and $\tau \equiv \varepsilon\{\int_0^x [d\zeta/c_g(\zeta)] - t\}$ (t being the physical time) are the coordinates in a frame moving at the envelope group velocity, $c_g \equiv \partial\omega/\partial k = (g/2\omega)[\sigma + \kappa(1-\sigma^2)]$.

Here $\tilde{\gamma} \equiv \gamma[c_g(\xi=0)/c_g(\xi)]$ is the shoaling-induced correction of the standard nonlinear coefficient γ, and β is the group-velocity dispersion. They only depend on κ [33], with $\beta < 0$ regardless of κ (only surface gravity waves are considered [33]) and $\tilde{\gamma} \geq 0$ for $\kappa \geq 1.363$, so that $\beta\tilde{\gamma} < 0$ (in this focusing regime c_g monotonically decreases, and shoaling only increases slightly the effective nonlinearity $\tilde{\gamma}$; see Supplemental Material Sec. S1 [36]).

The NLSE (1) conserves only the mass $N \equiv \int_{-\infty}^{\infty} |V|^2 d\tau$ and the momentum $P \equiv \mathrm{Im}\{\int_{-\infty}^{\infty} V^*(\partial V/\partial\tau)d\tau\}$, which we use in our numerical simulations to ensure the integration precision. Moreover, we introduce the quantities $A \equiv V/V_0$, $X \equiv \xi/L_{\mathrm{nl}}$, $T \equiv \tau/T_{\mathrm{nl}}$, where V_0 is the amplitude of the input plane wave (carrier), while $L_{\mathrm{nl}} = 1/(\tilde{\gamma}V_0^2)$ and $T_{\mathrm{nl}} = \sqrt{2|\beta|L_{\mathrm{nl}}} = \sqrt{2|\beta|/(\tilde{\gamma}V_0^2)}$ are the associated characteristic nonlinear length and temporal scales, respectively. This allows us to cast Eq. (1) into the dimensionless focusing NLSE:

$$i\frac{\partial A}{\partial X} - \frac{1}{2}\frac{\partial^2 A}{\partial T^2} - |A|^2 A = 0. \tag{2}$$

We let the depth increase from h^0 to $h^\infty > h^0$ over a a distance L_{step}, with $(h^\infty - h^0)/\varepsilon^2 \ll L_{\mathrm{step}} \ll L_{\mathrm{nl}}$, to prevent spurious reflections [26], while remaining essentially local compared to the envelope scale of variation L_{nl}. The normalization of Eq. (2) changes from before to after the bathymetry change. Assuming a fixed mass N (shoaling being negligible), two different families of solutions of Eq. (2) can be matched across the change (henceforth, superscripts 0 and ∞ denote the physical quantities before and after the change).

First, we consider the AB solution [22],

$$A_{\mathrm{AB}}(T,X) = \left[1 + \frac{\frac{(\Omega^0)^2}{2}\cosh bX + ib\sinh bX}{\sqrt{1 - \frac{(\Omega^0)^2}{4}}\cos\Omega^0 T - \cosh bX}\right] e^{iX}, \tag{3}$$

where Ω^0 is the initial normalized MI sideband detuning and $b \equiv \Omega^0\sqrt{1-(\Omega^0)^2/4}$ the linear MI gain. This solution exists only for $0 \leq \Omega^0 \leq 2$, is periodic in T, and evolves in X connecting two homogeneous plane wave states of unit amplitude at $X \to \pm\infty$ [Fig. 1(a)]. It thus corresponds to the separatrix of infinite-dimensional NLSE.

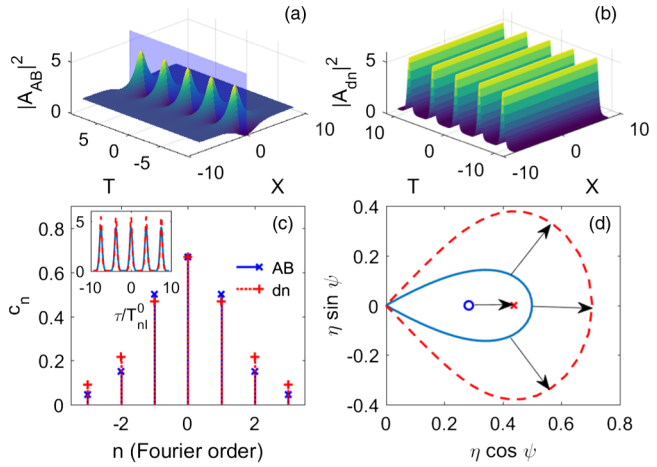

FIG. 1. Principle of AB conversion into a dnoidal solution of the NLSE. (a) Space-time evolution of the AB for a normalized detuning $\Omega^0 = 1.67$. (b) Dnoidal solution for normalized detuning $\Omega^\infty = 1.34$. (c) Best matching of Fourier coefficients of the AB [at the peak distance, blue shading in (a)] to the dnoidal solution. Inset: superimposed time profiles. (d) Phase plane trajectories of AB and dnoidal for Ω^0 (blue solid line and circle) and Ω^∞ (red dashed line and cross). Arrows show the effect of separatrix dilation.

Second, recall the dnoidal solutions [20],

$$A_{\mathrm{dn}}(T,X;m)=\alpha\,\mathrm{dn}[\alpha T;m]e^{i\chi^2 X}, \tag{4}$$

where $\alpha=\chi\sqrt{2/(2-m^2)}$, and χ a constant to be determined. The parameter $0<m<1$ implicitly defines the solution period: $T_{\mathrm{dn}}=2K/\alpha$, where $K\equiv K(m)$ is the complete elliptic integral of the first kind [37]. This solution has a steady amplitude profile and generalizes the soliton solution for T-periodic boundary conditions [Fig. 1(b)]. It is the infinite-dimensional counterpart of a center in a Hamiltonian system.

We seek m that matches the breather solution $A_{\mathrm{AB}}(T,X)$ to a steady profile $A_{\mathrm{dn}}(T,X;m)$ at a given stage X of the evolution. This will stabilize ("freeze") a strongly modulated nonlinear state.

Considering the phase invariance of the NLSE and the realness of the AB at its peak position $X=0$, we choose $A^0_{\mathrm{AB}}\equiv -A_{\mathrm{AB}}(T,0)$ to have positive maxima and negative minima [$A^0_{\mathrm{AB;max,min}}=1\pm\sqrt{4-(\Omega^0)^2}$], inset of Fig. 1(c) corresponding to the shaded blue plane of Fig. 1(a). We expand this real-valued wave form in Fourier series $A^0_{\mathrm{AB}}(T)=c^0_0+\sum_{n\neq 0}c^0_n e^{in\Omega^0 t}$ [38], with

$$c^0_0=(\Omega^0-1),\qquad c^0_n=\Omega^0\left(\frac{2-\Omega^0}{2+\Omega^0}\right)^{|n|/2} \tag{5}$$

[Fig. 1(c)]. The dnoidal profile that best matches A^0_{AB} must first be real valued like the AB. Therefore, we take $A^\infty_{\mathrm{dn}}(T)\equiv A_{\mathrm{dn}}(T,0)$. Second, the maxima $\alpha\geq 0$ at $T=kT_{\mathrm{dn}}$ and minima $\alpha\sqrt{1-m}\geq 0$ at $T=T_{\mathrm{dn}}/2+kT_{\mathrm{dn}}$ of $A_{\mathrm{dn}}(T,X)$ must coincide to those of the AB. Third, neglecting shoaling, the conservation of N implies $\alpha^2=K/E$ [37], where $E\equiv E(m)$ is the complete elliptic integral of the second kind. Finally, the normalized detuning in the MI band corresponding to a particular dnoidal solution is derived by well-known formulas [37], as $\Omega^\infty\equiv\pi\alpha/K=\pi[KE]^{-1/2}$.

The problem is thus reduced to finding the value of Ω^∞ that best matches $A^0_{\mathrm{AB}}(T)$ to $A^\infty_{\mathrm{dn}}(T)$. The latter expands in Fourier series:

$$c^\infty_0=\frac{\Omega^\infty}{2},\qquad c^\infty_n=\Omega^\infty\frac{q^{|n|}}{1+q^{2|n|}}, \tag{6}$$

with $q\equiv q(m)$ the elliptic *nome*.

We require that the main (continuous) components are equal; i.e., $c^0_0=c^\infty_0$. The comparison of Eqs. (5) and (6) yields

$$\Omega^\infty=2(\Omega^0-1), \tag{7}$$

providing the main theoretical result of our work. It simply links the two normalized pulsations across the depth change for optimally matching an AB to a steady dnoidal envelope. Clearly, the envelope matching requires that the physical sideband detuning f_m remains the same, whereas in Eq. (7) the pulsations $\Omega^{0,\infty}=2\pi f_m T^{0,\infty}_{\mathrm{nl}}$ differ on the two sides (0, ∞) because of the change in $T^{0,\infty}_{\mathrm{nl}}$, which accounts for the local depth. Thus, Eq. (7) is equivalent to $T^\infty_{\mathrm{nl}}=2T^0_{\mathrm{nl}}-(\pi f_m)^{-1}$ allowing us to determine κ^∞ given κ^0. Note also that $\Omega^\infty\geq\Omega^0$ for $0\leq\Omega^0\leq 2$: this is consistent with the requirement $h^\infty>h^0$, because T_{nl} decreases monotonically with κ and h; see the Supplemental Material Sec. S1 [36].

Figure 1(c) compares the spectra of the AB and the dnoidal, when Eq. (7) is fulfilled. The sidebands ($n\geq 1$) match satisfactorily. Small unavoidable discrepancies induce small oscillations around the dnoidal (matching more than one c_n is possible for the trivial case $\Omega^0=\Omega^\infty=2$ only, i.e., vanishing jump and MI band edge). This is also obvious from the phase-space representation of the matching process [(Fig. 1(d)], where the variables (ψ,η) are, respectively, the relative phase and sideband fraction of the two families of solutions (see Refs. [18,32,39] and the Supplemental Material Sec. S2 [36]). The optimal jump [Eq. (7)] leads the separatrix apex ($\psi=0$) before the jump (blue solid line) to closely approach the center (red cross) standing for the dnoidal after the phase-space dilation induced by the jump. Indeed, the nonperfect superposition of the (blue) separatrix apex and the (red) center is responsible for small oscillations around the dnoidal after the jump. These small oscillations around the maximum breather compression point are still nonlinear, because the energy is periodically exchanged between different sideband pairs. Note that this approach can be adapted to near-separatrix conditions, as detailed in Supplemental Material Sec. S3 [36].

Our approach establishes that AB freezing is favored for $\sqrt{3}<\Omega^0<2$, since A^0_{AB} stays positive like A^∞_{dn} (for $0\leq\Omega^0\leq\sqrt{3}$ the AB takes negative values, inaccessible to the dnoidal family). However, in Fig. 1 and in the experiment, we operate slightly below $\Omega^0=\sqrt{3}$ to increase the MI gain, but still the temporal profiles show a very good matching [inset of Fig. 1(c)].

Our theoretical results allow us to design an experimental realization in a the 30×1 m^2 water wave flume of The University of Sydney [Fig. 2(a)]. Rigid aluminium plates, each 2 m long, have been lifted from the bottom of the tank to allow a flat floor with constant depth $h^0=32.4$ cm up to the distance $x=12.35$ m and $h^\infty=55.2$ cm from $x=14.28$ m with a constant slope in between.

The initial conditions feature a carrier at a central frequency $f_0=1.53$ Hz slowly modulated with frequency (sideband detuning) $f_m=0.18$ Hz to form an AB focusing at $x=10.28$ m [40]. These carrier and modulation frequencies are within reach of the wave maker ($f\leq 2$ Hz). This implies $\kappa^0=3.06$ and $\kappa^\infty=5.02$, and

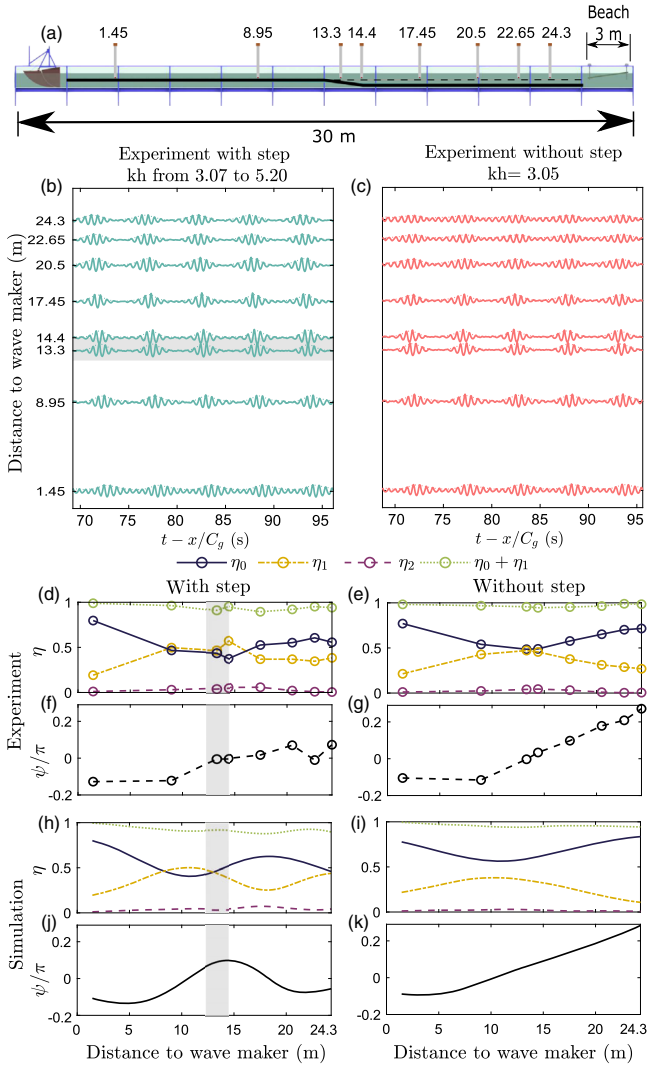

FIG. 2. (a) Water wave flume with artificial floor setup. One end shows the piston-type wave maker and the other end an inclined wave absorber with an artificial grass layer. Top: positions of the wave gauges. (b) Wave height at each recorded position for the experiment with variable bathymetry, multiplied by a factor 20; the gray stripe indicates the position of the step. (c) Wave height at each recorded position for the experiment with constant bathymetry, multiplied by a factor 20. (d)–(k) Sideband evolution of the AB-type surface water wave over the adopted bathymetry with the depth step (d),(f),(h),(j), and the constant flat bottom h^0 (e),(g),(i),(k). (d)–(g) Sideband dynamics as identified from the eight gauge measurements, connected by a linear interpolation; (h)–(k) corresponding NLSE-simulated evolution. (d),(e),(h),(i) Sideband fractions η_0, η_1, η_2 of modes at frequencies 0 (carrier), $\pm\Omega$, and $\pm 2\Omega$, respectively. (f),(g),(j),(k) Phase ψ of first-order sidebands (modes at $\pm\Omega$) relative to the carrier frequency, i.e., $\eta_0 \equiv |\hat{V}(\xi,0)|^2/N$, $\eta_1 \equiv [|\hat{V}(\xi,\Omega)|^2 + |\hat{V}(\xi,-\Omega)|^2]/N$, and $\eta_2 \equiv [|\hat{V}(\xi,2\Omega)|^2 + |\hat{V}(\xi,-2\Omega)|^2]/N$, and $\psi \equiv [(\phi_1 + \phi_{-1})/2] - \phi_0$, with $\phi_n \equiv \mathrm{Arg}[\hat{V}(\xi,n\Omega)]$, where $\hat{V}$ denotes the Fourier transform of V.

the initial steepness is $\varepsilon = 0.14$, most likely preventing wave breaking. With these parameters, we obtain $\Omega^0 = 1.67 < \sqrt{3}$, allowing us to observe one FPUT cycle within the tank length. Eight resistive wave gauges characterized the wave train evolution before, during, and after the depth transition. The first gauge is used to reconstruct, by conventional Hilbert transform and bound mode filtering [41], the envelope used for numerical integration of the NLSE [Eq. (1)], including linear dissipation resulting from inclined beds [42].

We compare the experimental traces with and without the bathymetry step. We observe that the former [Fig. 2(b)] still exhibits a train of clearly modulated pulses at the end of the tank, while the latter [Fig. 2(c)] qualitatively recurs to the initial state. This is particularly evident by comparing traces at $x = 22.65$ m and $x = 24.3$ m. This is the first strong evidence of stabilization.

In order to quantitatively reconstruct the phase-space trajectories described above and map them, we directly Fourier transform the surface elevation to extract the amplitude of the central mode and of the (unstable) $\pm\Omega$ and (stable) $\pm 2\Omega$ sidebands [Fig. 2(d)], as well as the relative phase ψ between the carrier and the unstable sidebands [Fig. 2(f)]. The $\pm\Omega$ sidebands grow until $x \approx 14$ m, i.e., where the depth step (gray band) stabilizes them to a relatively constant value, preventing the FPUT recurrence. The central mode evolves complementarily. Simultaneously, the relative phase of the first sideband pair stops growing. NLSE simulations reproduce quantitatively this behavior, with a stabilization of the sidebands to a high value and a stop to the growth of the sideband phase [Figs. 2(h) and 2(j)]. This behavior contrasts with both the measurements [Figs. 2(e) and 2(g)] and the simulation [Figs. 2(i) and 2(k)] on a uniform depth, for which the FPUT recurrence is expected to occur before the end of the flume while the relative phase ψ grows steadily. The small discrepancy between the focal point of the AB chosen as initial condition and the actual measured value ascribe to dissipation [24] and to higher-order physical effects, disregarded in the NLSE [43,44]. We interpret the small decay (growth) of η_0 (η_1) just after the depth jump as due to a partial reflection of the wave on the transition region, yielding imperfect energy transfer or to a small inaccuracy in gauge calibration.

Sidebands at $\pm 2\Omega$ stay below 6%. Therefore, we can safely rely on the reduced set of variables introduced originally in Ref. [18] and recently employed in nonlinear fiber optical experiments [19,39] (see Supplemental Material Sec. S2 [36]). In Fig. 3(a) we map the experimental trajectories onto the plane of Fig. 1(d) and compare them to simulated results. While over a flat bottom the system is ejected outside of the separatrix and displays unlocked phase growth, the bathymetry step forces the trajectory inside the separatrix, clearly shown by phase locking at $\psi \approx 0$.

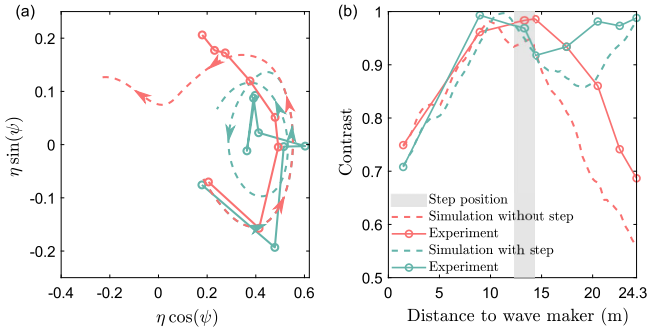

FIG. 3. (a) Propagation of a surface water wave AB over the depth step followed by flat bottom, displayed in the phase plane of Fig. 1(d), where $\eta \equiv \eta_1$ of Fig. 2. The respective NLSE simulations last up to 37.7 m. (b) Corresponding envelope contrast $C \equiv 1 - [\min|U|/\max|U|]$.

By estimating T_{nl} from the depth, carrier frequency, and the experimental value of $V_0\sqrt{N}$, we derive the normalized detuning values: before the step, at $x = 8.95$ m, $\Omega^0 \approx 1.67$, while after, at $x = 14.40$ m, the value of $\Omega^\infty \approx 1.34$ is indeed very close to the theoretical optimal as in Eq. (7).

The effect of the depth step is even more visible by looking at the contrast $C \equiv 1 - [\min|U|/\max|U|]$ of the temporal envelope modulation, averaged over all the modulation cycles comprised in the measured waveform [Fig. 3(b)]. The contrast rises to 1 in the AB focusing region ("inspiration" of the AB). On a flat bottom, it symmetrically decays after the focus (AB "expiration") due to the FPUT recurrence. Conversely, the bathymetry step locks the contrast to its maximum value. NLSE simulations reproduce well this behavior. Analogous experimental results can be achieved for near-AB conditions (see Supplemental Material Sec. S4 [36]).

To summarize, we have found a theoretical condition to dynamically stabilize unstable nonlinear waves. While the approach applies to any system described by the NLSE, and could therefore be easily generalized to other dynamical models, we have experimentally confirmed our finding for the specific case of wave hydrodynamics. A sharp change in water depth simultaneously modifies the dispersion and nonlinearity experienced by surface gravity wave packets, thus dramatically modifying their dynamical behavior. In the case of ABs, the separatrix expands and ends up enclosing the system trajectory, which is stabilized around an elliptic fixed point, i.e., a center. This jump can be described as the optimal matching of an initial AB solution to a steady dnoidal solution of the universal NLSE, illustrating the generality of this wave control process. This approach contrasts with that of a slow evolution of the system over several envelope oscillations, that also results in system stabilization [35], and from stabilization mechanisms relying on dissipation [45].

We anticipate that this cross-disciplinary approach will be further explored in other nonlinear dispersive media and will improve understanding of nonlinear wave control and transformation through a change of the waveguiding and consequently wave propagation characteristic parameters.

We acknowledge financial support from the Swiss National Science Foundation (Project No. 200020-175697) and the University of Sydney–University of Geneva Partnership collaboration award. We thank Debbie Eeltink for fruitful discussion. Zachary Benitez and Theo Gresley-Daines are acknowledged for the meticulous design of the experimental setup and technical support.

*jerome.kasparian@unige.ch
†andrea.armaroli@univ-lille.fr
Present address: PhLAM–Laboratoire de Physique des Lasers, Atomes et Molécules, IRCICA, 50 avenue Halley, 59658 Villeneuve d'Ascq, France.

[1] P. L. Kapitza, J. Exp. Theor. Phys. **21**, 588 (1951).
[2] S. K. Turitsyn, B. G. Bale, and M. P. Fedoruk, Phys. Rep. **521**, 135 (2012).
[3] T. M. Hoang, C. S. Gerving, B. J. Land, M. Anquez, C. D. Hamley, and M. S. Chapman, Phys. Rev. Lett. **111**, 090403 (2013).
[4] C. Rizza and A. Ciattoni, Phys. Rev. Lett. **110**, 143901 (2013).
[5] B. Eiermann, P. Treutlein, T. Anker, M. Albiez, M. Taglieber, K.-P. Marzlin, and M. K. Oberthaler, Phys. Rev. Lett. **91**, 060402 (2003).
[6] S. Fu, J. Zhou, Y. Li, L. Shemer, and A. Arie, Phys. Rev. Lett. **118**, 144501 (2017).
[7] G. Marcucci, D. Pierangeli, A. J. Agranat, R.-K. Lee, E. Del Re, and C. Conti, Nat. Commun. **10**, 5090 (2019).
[8] V. I. Arnol'd, *Mathematical Methods of Classical Mechanics*, 2nd ed. (Springer, New York, 2013).
[9] S. H. Strogatz, *Nonlinear Dynamics and Chaos: With Applications to Physics, Biology, Chemistry, and Engineering*, 2nd ed., Studies in Nonlinearity (Westview Press, Boulder, 2015).
[10] T. B. Benjamin and J. E. Feir, J. Fluid Mech. **27**, 417 (1967).
[11] V. E. Zakharov and L. A. Ostrovsky, Physica (Amsterdam) **238D**, 540 (2009).
[12] J. M. Dudley, G. Genty, A. Mussot, A. Chabchoub, and F. Dias, Nat. Rev. Phys. **1**, 675 (2019).
[13] T. Waseda, in *Ocean Wave Dynamics* (World Scientific, Singapore, 2020), pp. 103–161.
[14] V. E. Zakharov, J. Appl. Mech. Tech. Phys. **9**, 190 (1968).
[15] N. Akhmediev, V. Eleonskii, and N. Kulagin, Sov. Phys. JETP **62**, 894 (1985).
[16] M. J. Ablowitz and B. M. Herbst, SIAM J. Appl. Math. **50**, 339 (1990).
[17] H. T. Moon, Phys. Rev. Lett. **64**, 412 (1990).
[18] S. Trillo and S. Wabnitz, Opt. Lett. **16**, 986 (1991).
[19] A. Mussot, C. Naveau, M. Conforti, A. Kudlinski, F. Copie, P. Szriftgiser, and S. Trillo, Nat. Photonics **12**, 303 (2018).
[20] H. C. Yuen and B. M. Lake, Adv. Appl. Mech. **22**, 67 (1982).
[21] M. Magnani, M. Onorato, D. Gunn, M. Rudman, B. Kibler, N. Akhmediev, T. Waseda, and A. Chabchoub, Water Waves **2**, 113 (2020).

[22] N. N. Akhmediev and V. I. Korneev, Theor. Math. Phys. **69**, 1089 (1986).
[23] N. Akhmediev, Nature (London) **413**, 267 (2001).
[24] O. Kimmoun, H. C. Hsu, H. Branger, M. S. Li, Y. Y. Chen, C. Kharif, M. Onorato, E. J. R. Kelleher, B. Kibler, N. N. Akhmediev, and A. Chabchoub, Sci. Rep. **6**, 28516 (2016).
[25] F. D. Tappert and N. J. Zabusky, Phys. Rev. Lett. **27**, 1774 (1971).
[26] V. D. Djordjevic and L. G. Redekopp, J. Phys. Oceanogr. **8**, 1016 (1978).
[27] D. Dutykh, C. Labart, and D. Mitsotakis, Phys. Rev. Lett. **107**, 184504 (2011).
[28] K. K. Trulsen, H. Zeng, and O. Gramstad, Phys. Fluids **24**, 097101 (2012).
[29] P. J. Everitt, M. A. Sooriyabandara, M. Guasoni, P. B. Wigley, C. H. Wei, G. D. McDonald, K. S. Hardman, P. Manju, J. D. Close, C. C. N. Kuhn, S. S. Szigeti, Y. S. Kivshar, and N. P. Robins, Phys. Rev. A **96**, 041601(R) (2017).
[30] A. Bendahmane, A. Mussot, P. Szriftgiser, O. Zerkak, G. Genty, J. M. Dudley, and A. Kudlinski, Opt. Lett. **39**, 4490 (2014).
[31] N. Ercolani, M. Forest, and D. W. McLaughlin, Physica (Amsterdam) **43D**, 349 (1990).
[32] M. Conforti, A. Mussot, A. Kudlinski, S. Rota Nodari, G. Dujardin, S. De Biévre, A. Armaroli, and S. Trillo, Phys. Rev. Lett. **117**, 013901 (2016).
[33] C. C. Mei, M. Stiassnie, and D. K.-P. Yue, *Theory and Applications of Ocean Surface Waves: Nonlinear Aspects* (World Scientific, Singapore, 2005).
[34] M. Onorato, D. Proment, and A. Toffoli, Phys. Rev. Lett. **107**, 184502 (2011).
[35] A. Armaroli, A. Gomel, A. Chabchoub, M. Brunetti, and J. Kasparian, Nonlinear Dyn. **101**, 1131 (2020).
[36] See Supplemental Material at http://link.aps.org/supplemental/10.1103/PhysRevLett.126.174501 for the discussion of Eq. (1) and the main properties of its coefficients (Sec. S1), the technical details of the choice of phase-space variables and the three-wave reduced approach (Sec. S2), and additional numerical (Sec. S3) and experimental results (Sec. S4) involving near-AB initial conditions.
[37] P. F. Byrd and M. D. Friedman, *Handbook of Elliptic Integrals for Engineers and Scientists* (Springer, Berlin, 1971).
[38] A. Bendahmane, A. Mussot, A. Kudlinski, P. Szriftgiser, M. Conforti, S. Wabnitz, and S. Trillo, Opt. Express **23**, 30861 (2015).
[39] G. Vanderhaegen, P. Szriftgiser, A. Kudlinski, M. Conforti, S. Trillo, M. Droques, and A. Mussot, Opt. Express **28**, 17773 (2020).
[40] A. Chabchoub, T. Waseda, B. Kibler, and N. Akhmediev, J. Ocean Eng. Mar. Energy **3**, 385 (2017).
[41] A. R. Osborne, *Nonlinear Ocean Waves and the Inverse Scattering Transform* (Academic Press, New York, 2009).
[42] J. N. Hunt, La Houille Blanche **6**, 836 (1952).
[43] H. D. Zhang, C. Guedes Soares, and M. Onorato, Ocean Eng. **89**, 1 (2014).
[44] A. Armaroli, M. Brunetti, and J. Kasparian, Phys. Rev. E **96**, 012222 (2017).
[45] J. M. Soto-Crespo, N. Devine, and N. Akhmediev, Phys. Rev. A **96**, 023825 (2017).